

Special Section on STAG 2018

# Shape analysis of 3D nanoscale reconstructions of brain cell nuclear envelopes by implicit and explicit parametric representations

Marco Agus<sup>a,c,\*</sup>, Maria Veloz Castillo<sup>b</sup>, Javier F. Garnica Molina<sup>b</sup>, Enrico Gobetti<sup>c</sup>, Heikki Lehtälä<sup>d</sup>, Alex Morales Tapia<sup>a</sup>, Pierre J. Magistretti<sup>b</sup>, Markus Hadwiger<sup>a</sup>, Corrado Calì<sup>b,\*\*</sup>

<sup>a</sup> Visual Computing Center, King Abdullah University of Science and Technology, Thuwal 23955-6900, Saudi Arabia

<sup>b</sup> Biological and Environmental Science and Engineering Division, King Abdullah University of Science and Technology, Thuwal 23955-6900, Saudi Arabia

<sup>c</sup> Center for Advanced Studies, Research and Development in Sardinia (CRS4), Visual Computing Group, Cagliari, Italy

<sup>d</sup> CSC - IT Center for Science, Espoo, Finland

## ARTICLE INFO

### Article history:

Received 2 December 2018

Revised 16 May 2019

Accepted 19 May 2019

Available online 25 May 2019

### Keywords:

Shape analysis

Nanoscale cell reconstruction

Nuclear envelopes

Cell classification

## ABSTRACT

Shape analysis of cell nuclei is becoming increasingly important in biology and medicine. Recent results have identified that large variability in shape and size of nuclei has an important impact on many biological processes. Current analysis techniques involve automatic methods for detection and segmentation of histology and microscopy images, but are mostly performed in 2D. Methods for 3D shape analysis, made possible by emerging acquisition methods capable to provide nanometric-scale 3D reconstructions, are still at an early stage, and often assume a simple spherical shape. We introduce here a framework for analyzing 3D nanoscale reconstructions of nuclei of brain cells (mostly neurons), obtained by semiautomatic segmentation of electron micrographs. Our method considers two parametric representations: the first one customizes the implicit *hyperquadrics* formulation and it is particularly suited for convex shapes, while the latter considers a *spherical harmonics* decomposition of the explicit radial representation. Point clouds of nuclear envelopes, extracted from image data, are fitted to the parameterized models which are then used for performing statistical analysis and shape comparisons. We report on the analysis of a collection of 121 nuclei of brain cells obtained from the somatosensory cortex of a juvenile rat.

© 2019 The Authors. Published by Elsevier Ltd.

This is an open access article under the CC BY-NC-ND license.

(<http://creativecommons.org/licenses/by-nc-nd/4.0/>)

## 1. Introduction

In biology, the nucleus is a membrane-enclosed organelle found in eukaryotic cells, including the ones composing the brain. It is considered the control center of the cell, since, in particular, it organizes activities by regulating gene expression. The nuclear envelope, consisting of an inner and outer membrane separated by peri-nuclear space and perforated by nuclear pores, encloses the nucleus and separates it from the cytoplasm. All active and passive

transport processes in and out of the nucleus take place via the nuclear pores.

Recently, the analysis of proteins associated with the nuclear envelope in rat hippocampal neurons provided evidence that the shape of nuclei is an important factor influencing the nucleocytoplasmic exchange of macromolecules and ions, in particular calcium, which is a key regulator of neuronal gene expression [1]. Moreover, the size and shape of nuclear envelopes can vary not only among species, but also within species and even within a single individual, depending on cell types and other, even transient, conditions. Geometrically, the cell nucleus has been often studied as a spherical structure [2], but this approximation is increasingly proving way too coarse for a number of applications [1]. The analysis of shape properties is thus gaining importance in biology and medicine, since shape variability can provide indicators of different conditions and can provide hints for classifying cells.

A major field in which cell nucleus analysis is considered of paramount importance is computer-aided diagnostics [3], where

\* Corresponding author at: Visual Computing Center, King Abdullah University of Science and Technology, Thuwal 23955-6900, Saudi Arabia.

\*\* Corresponding author at: Biological and Environmental Science and Engineering Division, King Abdullah University of Science and Technology, Thuwal 23955-6900, Saudi Arabia.

E-mail addresses: [marco.agus@kaust.edu.sa](mailto:marco.agus@kaust.edu.sa) (M. Agus), [corrado.cali@kaust.edu.sa](mailto:corrado.cali@kaust.edu.sa) (C. Calì).

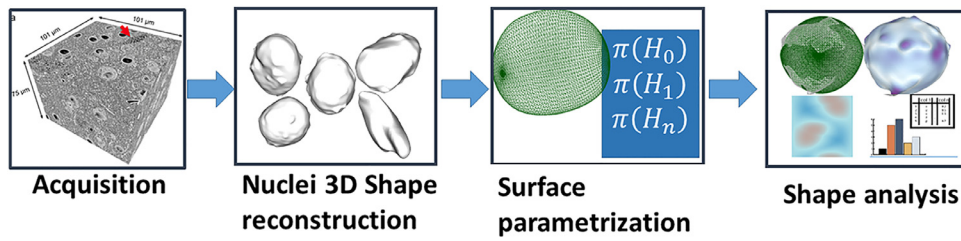


**Fig. 1.** Method overview: from 3D nanoscale reconstructions of neuron nuclei obtained from electron microscopy image stacks, we fit specific surface representations to derive parameter sets for shape analysis and classification.

a series of methods have been developed for automated 2D detection and segmentation on microscopy images, with the aim of providing support for various quantitative analyses, including calculating cellular morphology, including size, shape, or texture. However, most of nuclear analysis is performed directly on 2D images and only few efforts have used 3D reconstruction, in particular for studying the dynamics of nuclear infoldings in response to neuronal activity [4]. It is only very recently, with the emergence of digital acquisition methods capable to provide 3D reconstructions at nanometric resolution scale [5], that collections of 3D shape measurements of nuclei are starting to become available. There is a clear need to develop shape analysis frameworks to support domain scientists in performing 3D quantitative measures, classification and clustering operations, e.g., for associating different shapes to different nuclear conditions.

In this paper, we analyze digital 3D reconstructions of nuclei of brain cells that were obtained by segmenting serial electron micrographs at nanoscale resolution. We propose a shape analysis framework based on surface parameterizations, which provide simple but effective representations of nuclear envelope shapes. The parameters can be used for providing measures, features, and indicators for shape classification. To this end, we considered the hyperquadrics [6] implicit representation of convex shapes (see Fig. 1) using a formulation that provides us increased control in fitting the discrete point clouds representing the nuclei shapes as identified by image segmentation (see Section 4.1), and a more general function decomposition based on spherical harmonics [7], that provides ways to derive rotation-invariant shape descriptors (see Section 4.2). We show how the fitting for both parametric models can be computed using constrained optimization methods. For the hyperquadrics implicit representation we then create an explicit radial representation by sampling, which can be used for tessellation and shape comparison.

Our framework makes it possible to obtain parametric representations of shapes that can be used for measuring sizes, performing comparisons and for classifying nuclei to cell types and various conditions.

This article is an invited extended version of our STAG 2018 contribution [8], which was limited to the presentation of the hyperquadric approach. We here provide a more thorough exposition, but also significant new material, including the description of the acquisition method, the presentation of a refined pipeline supporting multiple fitting models, a generalized spherical harmonics solution, and additional qualitative and quantitative results. Also, we extended the classification options by comparing and evaluating the accuracy of different machine learning dimension reduction techniques.

The original framework was developed around a specific implicit representation, hyperquadrics, that was chosen after visual assessment of neural nuclei envelopes according to domain scientists indications. It proved to be more accurate than the usual spherical approximation for identifying convex neuronal nuclei. However, it was not optimal for concave and other

contorted shapes. By generalizing the framework by including the spherical harmonics basis decomposition [9], and deriving a parameterization of the explicit radial surface, we achieve increased performance on complex cases.

Here, we demonstrate the method on a collection of 121 brain cell nuclear envelopes. The input data came from semiautomatic segmentation of electron micrographs of a sample of somatosensory cortex of a juvenile rat coming from layers VI and II/III. We provide preliminary results of fitting performance of the proposed parametric models, as well as a discussion of a preliminary shape analysis performed by domain scientists with our framework.

## 2. Related work

We aim at creating a 3D shape analysis framework based on an implicit surface parameterization to be used for the study of 3D shapes obtained from nanoscale cell nuclear envelopes reconstructions. We discuss here the state-of-the-art in nuclei detection, shape analysis in neuroscience, and implicit representations in visual computing.

### 2.1. Cell nuclei segmentation

Accurate detection of individual cell nuclei in microscopy images is an essential and fundamental task for many biological studies. A comprehensive review of cell detection and segmentation algorithms can be found in [3]. The accuracy of segmentation and reconstruction determines the quality of morphology features extracted and is in some cases crucial for identifying and grading diseases. Broadly, three popular strategies are used for nucleus/cell segmentation:

- separate the foreground from the background, and split the object groups into individual nuclei or cells [10,11];
- identify markers of nuclei or cells, and then, expand the markers to the object boundaries [12–14];
- generate a sufficient number of region candidates, and then, select the best ones as final segmentation [15–17].

Very recently, Ram and Rodriguez [18] presented a cell nucleus detection system using the fast radial symmetry transform (FRST), to be used in fluorescence in-situ hybridization (FISH) images obtained via confocal microscopy. To the best of our knowledge, all published models are based on 2D segmentation of cell nuclei. Our method fits parametric representations to 3D reconstructions of cell nuclear envelopes. It extends a generic implicit surface model in a way that proves to be a simple but effective 3D parametric representation, expressive enough to perform statistical analysis and shape comparisons of rodent brain cell nuclear shapes.

### 2.2. Implicit representations in visual computing

A parametric representation of shape allows for the definition of geometrical objects using a few parameters and incorporating

prior knowledge. Because implicit surfaces can be designed so that the algebraic distance to them can be quickly computed by evaluating a simple differentiable function, they are better suited to fitting 2D and 3D data than the most common explicit models [19]. Implicit geometry has been used extensively for various applications, ranging from constructive solid geometry [20], to geometric modeling [21], to real time ray tracing [22,23], to molecular dynamics [24,25]. One of the most common implicit representations is the superquadric, introduced by Barr [26] and then widely applied to many problems, such as object representation [27], shape recovery [28], image segmentation [29], and object modeling [30].

Superquadrics are, however, constrained to represent symmetrical-section volumes. This limitation was removed by Hanson [6] with the introduction of the hyperquadric primitives, which include quadrics and superquadrics as special cases. Hyperquadrics are not symmetric and support taperings and distortions that are not normally present within the conventional superquadric framework. The application of hyperquadrics can be mainly found in shape recovery [31], but also in fitting models to sparse data [32]. Their 2D versions were used for 2D segmentation of nuclei shapes in nuclei observed with an epi-fluorescence microscope [33].

In this paper, we customize the hyperquadrics formulation for building a 3D shape analysis framework targeted to 3D nanoscale representations of brain cell nuclear shapes. We further generalize the approach by considering spherical harmonics, which have often been employed for representing spherical functions [34], but not previously in the context of nuclear shape fitting.

### 2.3. Shape analysis in neuroscience

The availability of 3D reconstructions of brain structures is driving the development of various frameworks for shape analysis in order to classify and account for variability to be associated to different structures and conditions. For a recent overview of the main methods employed in the analysis of brain structures, we refer reader to [35]. In general, shape analysis methods are mainly targeted to the full cortex acquired with MRI methods [36]. Recently, a study for 3D morphological analysis of asymmetric neuronal morphogenesis in developing zebrafish has been proposed [37], but wider application of shape analysis studies of brain structures at nanometric resolution are still lacking [5].

In the context of the specific analysis of nuclear envelopes, Queisser et al. [1] developed a tool to retrieve the 3D view of cell nuclei from laser scanning confocal microscopy data. Their method extracts surface information of the membrane by creating an iso-surface with a marching tetrahedra algorithm combined with a modified Dijkstra graph-search algorithm, and it has been used to show how synaptic activity induces dramatic changes in the geometry of the cell nucleus [4]. Recent methods on 3D morphometric analysis consider frequency decomposition frameworks [38], or functional spaces like Wasserstein space [39], or Random Markov Fields [40], and they are mostly used for studying hippocampal shapes [40] or full cortex affected by Alzheimer's disease [39].

Here we focus on 3D reconstructions of brain cell nuclei, and, to the best of our knowledge, our method is the first attempt of 3D shape analysis based on implicit parameterization.

## 3. Method overview

The full pipeline of the proposed shape analysis framework is schematized in Fig. 1. The first stage is data acquisition, which is carried out by digital imaging of brain samples using electron microscopes is followed by nuclear 3D shape reconstruction and parametric model fitting. Finally, the shape parameters are used for performing analysis and classification. The rest of the methods

section details the various components of the pipeline and presents the proposed parametric models in detail.

### 3.1. Data acquisition

A number of automated serial electron microscopy techniques have recently been developed, driven by the need of imaging large portions of the brain from different species. State-of-the-art EM setups can nowadays automatically cut serial sections and image them to produce aligned stacks with minimal human supervision. The use of electron micrographs also makes it possible to visualize even the finest lamelliform processes.

The general workflow for 3D reconstruction and visual analysis of brain structures is represented in Fig. 2. It begins with sample preparation and 3DEM [41] imaging. Acquisition of biological tissues can be performed automatically at a z-resolution of 5–50 nanometers depending on the cutting technique [41]. After imaging, image stack needs preprocessing prior the 3D reconstruction of the various cellular structures. First, the image stack needs to be aligned [42]. Following image registration, the stack is then segmented by means of manual or semi-automatic segmentation techniques [43]. Automated and semi-automatic segmentation techniques reduce tremendously the time and effort needed to generate a first-pass three-dimensional model. Finally, the model then needs to be proofread and corrected manually to achieve best results. The created dataset is composed of high-resolution, segmented image stacks that can be visualized, explored and analyzed with a variety of tools based on either volume data representation, or surface mesh generated from the segmentations.

Many neuroscientists take advantage of commercial or free software solutions [44,45] to perform the reconstruction. In our case, we currently rely on available semi-automatic solutions, such as *ilastik* [45] that aims for a segmentation accuracy comparable to what is obtainable with manual tools [44]. The specific pipeline employed to generate the data used in this work was designed by combining the complementary strengths of *ilastik* and *TrakEM2* [46], since *ilastik* is good for quickly finding the gross features and processes of a cell, while the manual approach of *TrakEM2* is good for specifying exact boundaries and finer details. A practical solution was also designed for dealing with large datasets on a single machine by subdividing them in piecewise chunks to fit with the *ilastik* semi-automated segmentation module called carving, which was accordingly refactored [47]. The semiautomatic segmentation method was used to label EM images, while surface reconstruction was performed on labelled masks by using marching tetrahedra [48]. Finally, for each reconstructed nuclear envelope surface, the vertices were collected as input point clouds for the shape analysis framework.

### 3.2. Problem statement

Given a 3D point cloud representing a closed shape of a cell nucleus, we can define our fitting/analysis problem as finding the parameters of a surface model which better approximates the point cloud. In general, the fitting/analysis method is composed of three tasks:

- define and compute the parameters of the chosen representation;
- evaluate fitting by tessellating the fitting surface through an explicit representation;
- use the extracted parameters for statistical computations and analysis, and create a predictive model for classifying different cell nuclei at varying conditions.

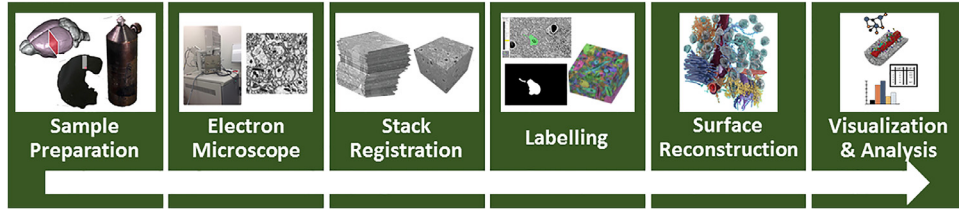


**Fig. 2.** Reconstruction workflow: from brain samples, high resolution micrographs are acquired through automatic cutting, aligned, and labelled through manual or semi-automatic segmentation techniques. Finally, high resolution surfaces are reconstructed from labelled volumes and used for visualization and analysis.

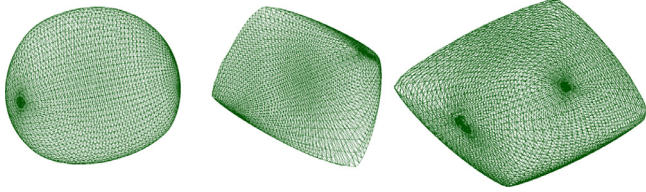


**Fig. 3.** Hyperquadrics examples: at varying of parameters of Eq. (1), various surfaces can be represented.

### 3.3. Shape modeling

In this work we considered two different parameterizations of nuclear shapes: the first one was chosen starting from qualitative assessment of nuclear shapes performed by domain scientists, that led to the hypothesis that implicit closed *hyperquadrics* [6] could provide effective representations of convex nuclear envelopes. In addition, a more general explicit parameterization was derived by considering the general spherical harmonics decomposition to represent the radial surface  $\rho = \rho(\theta, \phi)$  in spherical coordinates. The latter has been chosen since it has the advantage that the various components form an orthonormal basis for functions defined on the unit sphere, and in theory they should provide a compact description of shapes with fewer coefficients.

#### 3.3.1. Hyperquadrics representation

Given a 3D surface, a surface representation can be defined implicitly as the function  $H(x, y, z)$  such that the points of the surface respect the equation  $H(x, y, z) = 1$ . Hyperquadrics are implicit models defined by a sum of an arbitrary number of linear terms raised to powers, generating shapes whose bounding polytopes have an arbitrary number of faces [49].

A hyperquadric model is thus defined by the set of points satisfying:

$$H(x, y, z) = \sum_{i=1}^n \|H_i(x, y, z)\|^{\gamma_i} = 1, \quad (1)$$

where  $H_i(x, y, z) = a_i x + b_i y + c_i z + d_i$ .

At varying of parameters defining the individual components, different convex shapes can be represented (see Fig. 3). The requirements for having closed surfaces are that the exponents  $\gamma_i$  are positive, and that  $\|H_i(x, y, z)\| \leq 1$ . The geometric meaning is that for each component, all points of the surface are contained between the plane strip represented by equations  $H_i(x, y, z) = 1$  and  $H_i(x, y, z) = -1$  (see Fig. 4).

#### 3.3.2. Spherical harmonics decomposition

Spherical harmonics are a natural choice of basis functions for representing any twice-differentiable spherical functions [34]. They are an infinite set of complex functions that are single-valued, continuous, orthonormal, and complete on the sphere. They are defined as complex functions with respect to the order  $l$  and degree

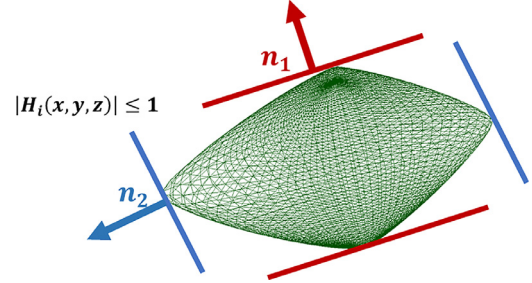


**Fig. 4.** Hyperquadric definition: for each component, all points of the surface are contained between the plane strip represented by equations  $H_i(x, y, z) = 1$  and  $H_i(x, y, z) = -1$ .

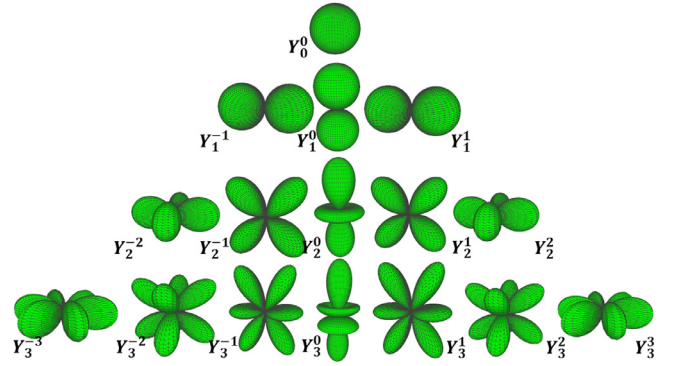


**Fig. 5.** Spherical harmonics: they are complex functions depending on order  $l$  and degree  $m$ , and they represent an orthonormal basis for decomposing radial functions.

$m$  in the following way:

$$Y_l^m(\theta, \phi) = \sqrt{\frac{2l+1}{4\pi} \frac{(lm)!}{(l+m)!}} P_l^m(\cos \theta) \exp im\phi \quad (2)$$

where  $l$  and  $m$  are integers such that  $|m| \leq l$ , and  $P_l^m$  are associated Legendre polynomials [9]. In Fig. 5 the 3D graphic representations of spherical harmonics up to order  $l = 3$  are shown. Any spherical function  $f(\theta, \phi)$  can be represented by a linear combination of spherical harmonics  $Y_l^m(\theta, \phi)$  as follows:

$$f(\theta, \phi) = \sum_{l=0}^{\infty} \sum_{m=-l}^l a_l^m Y_l^m(\theta, \phi). \quad (3)$$

This spherical harmonic expansion can be interpreted as the Fourier transform for functions defined on the sphere, converting spherical scalar signals into their frequency spectrum. Spherical harmonics have several interesting properties such as orthonormality, completeness, and coarse-to-fine hierarchy, which make them an effective choice of basis functions to represent radial surfaces  $\rho(\theta, \phi)$  [34].



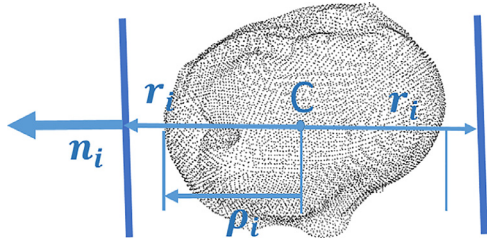


**Fig. 6.** Hyperquadric parameterization: the center of mass of the point cloud  $C$  is the origin of the reference system. For each patch  $H_i$ , plane strip width  $r_i$  is parametrized by applying a scale factor  $\sigma_i$  to the bounding distance  $\rho_i$  which is computed by projecting the point cloud with respect to the plane normal  $n_i$ .

#### 4. Point cloud fitting

Point cloud fitting consists of finding the optimal values for the parameters of a given model, which better approximate a set of points known to be on its boundary. In this section, we describe our approach to efficiently perform this task, on both the implicit hyperquadrics model and the radial explicit spherical harmonics decomposition.

##### 4.1. Hyperquadrics fitting

Given the equation of the hyperquadrics, each component can be parametrized with respect to the point cloud to fit. The original formulation (see Eq. (1)) describes each component as a plane equation represented by coefficients  $(a_i, b_i, c_i, d_i)$ , which are difficult to manage since they can vary indefinitely and they have no specific physical meaning. Hence, in order to reduce the number of parameters and to have better control of constraints, we derived a specific parameterization. We considered the center of mass of the point cloud  $C$  as origin of the reference system (see Fig. 6). Thus, the components  $H_i(x, y, z)$  can be written as

$$n_{xi}x + n_{yi}y + n_{zi}z = r_i, \quad (4)$$

where  $n_i = (n_{xi}, n_{yi}, n_{zi}) = (\cos \phi_i \cos \theta_i, \sin \phi_i \cos \theta_i, \sin \theta_i)$  is the unit vector representing the plane normal, and  $r_i$  is the plane distance from the center of mass. The latter can be further parametrized as  $r_i = \rho_i(1 + \sigma_i)$ , where  $\rho_i$  is the bounding distance for the point cloud with respect to the normal  $n_i$ , and  $\sigma_i$  is a scale factor for stretching or compressing the plane strip (see Fig. 6). Given that the bounding distance  $\rho_i$  can be computed for each plane with respect to the point cloud, for each patch  $H_i$  of the hyperquadrics we can control the width of the plane strip just by modifying the scale factor  $\sigma_i$ . Finally, the exponent factor can be written as  $\gamma_i = 2\epsilon_i$  in order to remove the norm operation. In this way, each component  $H_i(x, y, z)$  can be represented by four parameters:

$$\pi(H_i) = (\phi_i, \theta_i, \sigma_i, \epsilon_i) \quad (5)$$

##### 4.1.1. Least-squares problem

Given a point cloud  $(p_1, p_2, \dots, p_K)$ , the problem of fitting an hyperquadric surface can be expressed as a non-linear optimization problem where the target is to find the optimal parameterization  $\Pi(H) = (\pi(H_1), \pi(H_2), \dots, \pi(H_N))$  that minimizes the distance of the samples with respect to the surface represented by implicit function  $H(x, y, z)$ :

$$\Pi(H) = \arg \min_{\Pi} \sum_{k=1}^K d^2(p_k, H), \quad (6)$$

where the distance between a given sample  $p_k$  and the surface can be computed algebraically,

$$d_a^2(p_k, H) = (H(x_k, y_k, z_k) - 1)^2, \quad (7)$$

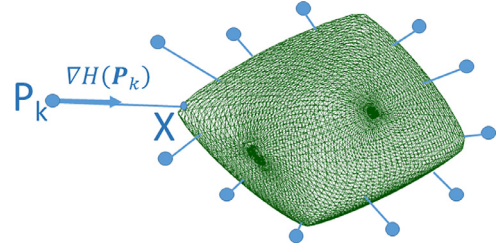


**Fig. 7.** Least-squares problem: the optimal implicit parameterization is found by minimizing the square distance of the input points with respect to the algebraic surface. Euclidean distance is approximated by using first order Taylor expansion.

but better accuracy can be obtained by estimating the Euclidean distance between the sample  $p_k$  and the hyperquadric surface (see Fig. 7). Specifically, considering the first-order Taylor expansion of the hyperquadric function, we have

$$H(x) \approx H(p_k) + \nabla H(p_k) \cdot (x - p_k), \quad (8)$$

and imposing  $H(x) = 1$ , we get

$$d^2(p_k, H) = \|x - p_k\|^2 \approx \frac{d_a^2(p_k, H)}{\|\nabla H(p_k)\|^2}, \quad (9)$$

that can be used for computing the cost function. To this end, we note that the gradient operator can be computed in analytic form from the hyperquadric definition:

$$\nabla H(x, y, z) = \sum_i \gamma_i (a_i x + b_i y + c_i z + d_i)^{\gamma_i - 1} (a_i, b_i, c_i). \quad (10)$$

For solving the constrained minimization problem, we consider the Levenberg–Marquardt method [50], using as a first guess an ellipsoid approximation with the plane normals and distances computed with respect to the oriented bounding box of the input point cloud [51]. For each iteration, bounding distances of plane strips are computed with respect to the plane normals defined by parameters  $\phi_i, \theta_i$ , and the scale factors  $\sigma_i$  are applied over it.

##### 4.1.2. Explicit radial representation

While the implicit representation recovered in the previous parts provides a very good shape descriptor, for a number of tasks, e.g., tessellation, it is handy to also have an equivalent explicit representation, capable to generate 3D points given a few parameters. However, given an implicit representation of an hyperquadric, there is no way to recover an explicit representation in closed form. We thus compute, through numerical optimization, a best fit spherical coordinates formulation

$$\begin{cases} x = \rho(\theta, \phi) \sin \theta \cos \phi \\ y = \rho(\theta, \phi) \sin \theta \sin \phi \\ z = \rho(\theta, \phi) \cos \theta \end{cases} \quad (11)$$

where the function  $\rho(\theta, \phi)$  varies according to the angles, and needs to be computed for a given sampling of the unit sphere. In our case, we consider a regular sampling, and for each pair of angles  $(\theta, \phi)$  we solve an optimization problem with Levenberg–Marquardt to find the optimal radius  $\rho$  such that the algebraic distance from the implicit function is minimal:

$$\rho(\theta, \phi) = \arg \min_{\rho} (H(x, y, z) - 1)^2. \quad (12)$$

Fig. 8 shows a schematic representation of the optimization process and the graphic representation of the explicit parameterization of an hyperquadric implicit function. The created samples are used for tessellating the hyperquadrics surface, for evaluating the fitting errors, and for visual comparisons with respect to the original shape.

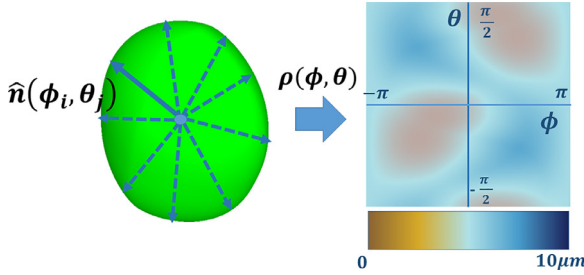


**Fig. 8.** Explicit radial representation: given the implicit representation of an hyperquadric, the explicit representation is computed by using spherical coordinates and computing radii on a regular sampling basis.

#### 4.2. Spherical harmonics fitting

In the case of fitting a point cloud to a spherical harmonic decomposition, we define a radial surface representation  $\rho_{L_{\max}}(\theta, \phi)$  in spherical coordinates as a truncated linear combination of spherical harmonic real components, by limiting the maximum degree to a specific value  $L_{\max}$ , in a way to have a fixed number of coefficients  $k = (L_{\max} + 1)^2$ :

$$\rho(\theta, \phi) \approx \rho_{L_{\max}}(\theta, \phi) = \sum_{l=0}^{L_{\max}} \sum_{m=-l}^l a_l^m \Re(Y_l^m(\theta, \phi)), \quad (13)$$

where  $\Re(Y_l^m(\theta, \phi))$  is the real part of the harmonic function. In order to obtain the SH coefficients  $a_l^m$  from the point cloud  $(p_1, p_2, \dots, p_n)$ , we convert the point samples in spherical coordinates  $(\rho_i, \theta_i, \phi_i)$  by using the inverse spherical transform

$$\begin{cases} \rho_i = \sqrt{x_i^2 + y_i^2 + z_i^2} \\ \theta_i = \arctan(\frac{\sqrt{x_i^2 + y_i^2}}{z_i}) \\ \phi_i = \arctan(\frac{y_i}{x_i}), \end{cases} \quad (14)$$

##### 4.2.1. Least-squares problem

The least-squares problem that we need to solve for fitting should minimize the squared distance between the points and the SH decomposition [34]. We can write Eq. (13) in matrix form  $Ya = R$ :

$$\begin{bmatrix} y_{1,1} & y_{1,2} & \dots & y_{1,n} \\ y_{2,1} & y_{2,2} & \dots & y_{2,n} \\ \dots & \dots & \dots & \dots \\ y_{k,1} & y_{k,2} & \dots & y_{k,n} \end{bmatrix} \begin{bmatrix} a_1 \\ a_2 \\ \dots \\ a_k \end{bmatrix} = \begin{bmatrix} \rho_1 \\ \rho_2 \\ \dots \\ \rho_n \end{bmatrix}, \quad (15)$$

where  $y_{i,j} = \Re(Y_l^m(\theta_i, \phi_i))$ ,  $a_j = a_l^m$ , with  $j = l^2 + l + m + 1$ ,  $k = (L_{\max} + 1)^2$ , and  $\rho_i = \rho(\theta_i, \phi_i)$ . For smoothing the solution, we also added a Tikhonov regularization term  $\Gamma$  [52], increasingly penalizing the coefficients as long as the order  $l$  increases, in a way that the least square problem is defined as:

$$a = \arg \min_a (\|Ya - R\|^2 + \nu \|\Gamma a\|^2), \quad (16)$$

leading to the following linear system

$$(Y^T Y + \nu C) a = Y^T R, \quad (17)$$

where  $C = \Gamma^T \Gamma$ :

$$C = \begin{bmatrix} l_j^2(l_j^2 + 1)^2 & & & \\ & \dots & & \\ & & \dots & \\ & & & l_{\max}^2(l_{\max}^2 + 1)^2 \end{bmatrix}, \quad (18)$$

where  $l_j$  is the spherical harmonics order associated with the coefficient  $j$ . In all results of this paper, we used a small regularization value ( $\nu = 10^{-5}$ ).

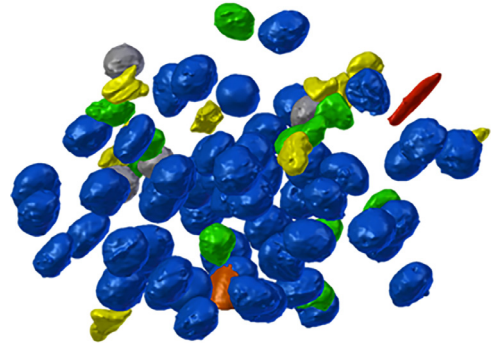


**Fig. 9.** Input nuclei envelopes: the analysis framework was tested on a collection of 97 3D reconstructions of brain cell nuclei extracted from a sample of layer VI somatosensory cortex of a juvenile rat (Fig. 10).

##### 4.2.2. Explicit radial representation

For tessellating, as opposed to the hyperquadric representation, the Spherical Harmonic decomposition has the advantage of providing directly an explicit representation which can be directly used for sampling the approximating shape.

#### 5. Implementation and results

**Implementation.** Our framework was implemented in C++, by adapting the levmar implementation of the Levenberg–Marquardt algorithm as iterative solver [50] for computing hyperquadrics parameters (we used OpenMP for parallelizing the projection computation), and by using eigen library [53] for linear least square optimization in the case of spherical harmonics parameters. For the fitting procedure we used the following constraints for the hyperquadrics patch parameters:  $-\pi \leq \phi_i \leq \pi$ ,  $-\frac{\pi}{2} \leq \theta_i \leq \frac{\pi}{2}$ ,  $-0.1 \leq \sigma_i \leq 0.5$ ,  $0.75 \leq \epsilon_i \leq 2.5$ . On the other side, the coefficients of spherical harmonics components were found by solving the linear system in Eq. (17) (with regularization factor  $\nu = 10^{-5}$ ). All fitting sessions were performed on a PC equipped with two CPU Intel Xeon 2,3 GHz and 128 GB RAM and running Windows 8. We also used the parameters derived from the explicit and implicit model for classifying the nuclei according to standard machine learning methods, that we implemented using Jupyter notebooks [54] and the scikit-learn [55] Python library.

**Biologic material.** Our test set was a collection of 121 3D reconstructions of brain cells nuclei. Of these, 97 were extracted from dense reconstructions coming from a semiautomatic segmentation of nanometric scale electron microscopy stacks, obtained after imaging a volume of brain parenchyma from layer VI somatosensory cortex of a P14 rat using a serial block-face scanning electron microscopy (SBEM) with a 3View module (Fig. 10 left). They were manually assigned to known cell types (Fig. 9). The additional two groups of 16 and 8 nuclear envelopes were instead extracted after imaging two different volumes of somatosensory cortex of the same rat. In these cases, the blocks were extracted from layer II/III. We used them as testing data for assessing the classifiers built on top of the shape parameterizations. In the following these nuclear envelope groups will be indicated as void and unknown. The Table 1 lists further details about this collection of nuclear shapes.

##### 5.1. Fitting evaluation

Given the collection of nuclear point clouds, we evaluated the quality of fitting by considering a hyperquadrics implicit representation containing various number of patches ( $N = 3, 4, 5, 6$ ), and various explicit spherical harmonics decompositions ( $L_{\max} = 2, 3, 5, 10, 20$ ). In the following, we will denote the

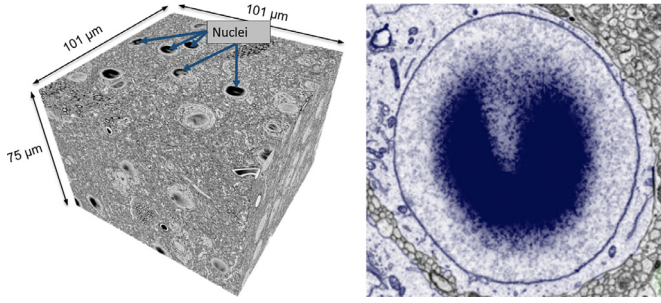


**Fig. 10.** Dataset acquisition. Left: dataset obtained by imaging a sample from the somatosensory cortex of a juvenile rat, using a serial block-face scanning electron microscopy (SBEM) with a 3View module. Right: neuronal nuclei present the dark artifact typical of electrons accumulating in portions of the sample where there is low density of biological material.

**Table 1**

*Nuclei statistics:* listing showing the number of nuclear envelopes, the average number of vertices, the volume size in  $\mu\text{m}^3$  with the standard deviation, and the surface size in  $\mu\text{m}^2$  with the standard deviation.

Type	# Cells	# Vertices	Volume( $\mu\text{m}^3$ )	Surface( $\mu\text{m}^2$ )
Neurons	58	9262	$715.7 \pm 102.5$	$408 \pm 34.5$
Astrocytes	10	9519	$354.29 \pm 63.7$	$270.8 \pm 25.8$
Endothelium	4	9235	$67.08 \pm 21.5$	$168.2 \pm 41.9$
Microglia	12	7780	$185.5 \pm 64.8$	$194.5 \pm 42.1$
Oligodend.	4	7225	$427 \pm 49.8$	$288 \pm 24.1$
Pericytes	10	10085	$107.2 \pm 39.3$	$159.9 \pm 28.8$
Void(LII/III)	16	771	$440.1 \pm 253.4$	$363.8 \pm 101.7$
Unkn(LII/III)	8	658	$297 \pm 264$	$250 \pm 110.2$

various cases with  $HQ_{N,C}$  and  $SH_{L,C}$ , where C is the number of coefficients.

Table 2 shows the statistics about the nuclear envelopes which were fitted. Specifically, we compare the two parameterizations in two situations: a case with the same number of coefficients ( $HQ_{4,16}$  and  $SH_{3,16}$ ), and a case with the same average accuracy ( $HQ_{5,20}$  and  $SH_{20,441}$ ). For the various cell categories, we report on the average mean error and on the fitting time. For each nuclear envelope, we used two evaluation metrics: the average error for the points in the shape (computed by using Eq. (9)), and the percent of points whose distance error is below  $0.5\mu\text{m}$ . Fig. 11 shows boxplots of these error metrics for the various cell categories using same parameter configurations in Table 2: in the top two graphs, the two parameterizations use the same number of coefficients ( $HQ_{4,16}$  and  $SH_{3,16}$ ), while in the bottom graphs the two models have similar average accuracy. From Table 2 and Fig. 11, it appears that, for both representations, the fitting is more accurate for neuron nuclei, while it is less accurate for shapes with irregular surface like microglia or pericytes. In general, we can also see that if we use representations with same number of coefficients, the hyperquadrics parameterization is generally more accurate.

For visual reference, Fig. 12 shows some examples of fitting obtained with the implicit and explicit model for various kinds of nuclear shapes. For each original input shape, we show tessellations of various fitted representations (either hyperquadrics and spherical harmonics), as well as their fitting errors, color-mapped over the original shape through the BuPu colorbrewer scheme [56] (color scale from 0 to  $0.5\mu\text{m}$ ). From Fig. 12, it appears that both parametric models are accurate for convex shapes, like neurons, or astrocytes cells (see on the left in Fig. 12), while they suffer in cases where the original shapes are irregular, like microglia or pericytes (see on the right in Fig. 12). Finally, in Fig. 13, we compare the mean fitting error and the processing time of the two parameterizations, at varying number of coefficients. We can see that, when using the same number of coefficients used for

generating the parametric description, the implicit hyperquadrics formulation appears to be slightly more accurate than the spherical harmonics decomposition. On the other hand, the orthonormal basis definition of spherical harmonics decomposition leads to a linear least square optimization method, which is an order of magnitude faster than the non-linear Levenberg–Marquardt method used for fitting hyperquadrics representations.

We can also notice that increasing the order of the spherical harmonics decomposition has diminishing returns, due to the standard spherical parameterization used in this work. To overcome this issue, we plan in future to explore more sophisticated reparameterizations involving connectivity and preserving lengths and surface areas.

## 5.2. Nuclei analysis

In addition to providing compact models usable for visualization, one of the main motivations of our fitted representations was that they may be helpful to directly and efficiently support various analysis tasks. In the following, we describe how our fitted representations were applied for the classification of nuclear shapes to cell types.

### 5.2.1. Preliminary classification

Domain scientists traditionally classify cells and their nuclear envelopes through visual assessment of morphological features visible in electron micrographs. Even when cell morphology is not visible, the plain nuclei have characteristic features that indicate the probable cell type. The nuclei of neurons tend to be almost spherical and are typically largest among all brains cells.

Interestingly, all neuronal nuclei in our sample showed a dark artifact that is typical of electron accumulation to areas of poor conductivity that comes from the lack of biological material, an effect that is also true for lumen of blood vessels (Fig. 10 right).

On the other hand, astrocyte nuclei have a more irregular shape, and are smaller than in neurons. The microglial nuclei are again smaller than in neurons and tend to be heavily squashed.

Statistical analysis is usually applied to the volume and the surface area of nuclei. For our sample set, the volume size computation showed that neurons had the biggest nuclei, followed by astrocytes and oligodendrocytes (see Fig. 14 and Table 1).

### 5.2.2. Classification using parametric representations

We hoped to improve these approximate classifications by applying our hyperquadrics and spherical harmonics fitting to nuclear envelope shapes. We used the classical support vector machine (SVM) [58,59] with radial basis function for deriving predictive models. We performed transformation of coefficients to remove dependencies arising from different orientations. For hyperquadrics fitting, we first ordered the components according to the exponent value, then aligned the plane normal components with respect to the first planar patch, and finally converted the angular values to normalized vector coefficients. After transformation, for hyperquadric representations composed of N patches, we obtained  $C = 2N + 3(N - 1) = 5N - 3$  rotation-invariant coefficients. For spherical harmonics parameterization, we applied the rotation-invariant energy descriptors proposed by Kazhdan et al. [7]. For each frequency  $l$  of the spherical harmonics decomposition, we computed rotation-invariant energies  $\{\epsilon_l, l = 0, \dots, L_{\max}\}$  starting from coefficients:

$$\epsilon_l = \sum_{m=-l}^l \|a_l^m\|^2. \quad (19)$$

For a spherical harmonics decomposition of order  $L_{\max}$  we created  $C = L_{\max} + 1$  rotation-invariant coefficients. In the following

**Table 2**

*Nuclei fitting statistics:* we compare hyperquadrics and spherical harmonics in two situations: a cases with the same number of coefficients ( $HQ_{4,16}$  and  $SH_{3,16}$ ), and a case with the same average accuracy ( $HQ_{5,20}$  and  $SH_{20,441}$ ). For various cell categories, we list the mean accuracy error per vertex and the average processing time.

Type	$HQ_{4,16}$ Err( $\mu$ m)	$SH_{3,16}$ Err( $\mu$ m)	$HQ_{4,16}$ Time(s)	$SH_{3,16}$ Time(s)	$HQ_{5,20}$ Err( $\mu$ m)	$SH_{20,441}$ Err( $\mu$ m)	$HQ_{5,20}$ Time(s)	$SH_{20,441}$ Time(s)
All	0.353	0.437	57.43	0.021	0.338	0.338	64.53	0.672
Neurons	0.203	0.296	67.17	0.027	0.191	0.266	66.28	0.842
Astrocytes	0.309	0.449	51.00	0.028	0.32	0.368	101.6	0.834
Endothelium	0.868	0.781	103.59	0.027	0.913	0.642	134.29	0.827
Microglia	0.487	0.596	76.88	0.022	0.404	0.39	87.2	0.687
Oligodend.	0.161	0.198	99.8	0.029	0.152	0.176	59.32	0.934
Pericytes	0.524	0.819	74.59	0.021	0.508	0.462	103.01	0.704
Void-LII/III	0.554	0.483	6.15	0.002	0.517	0.371	6.563	0.095
Unkn.-LII/III	0.512	0.655	4.286	0.002	0.543	0.454	6.01	0.083

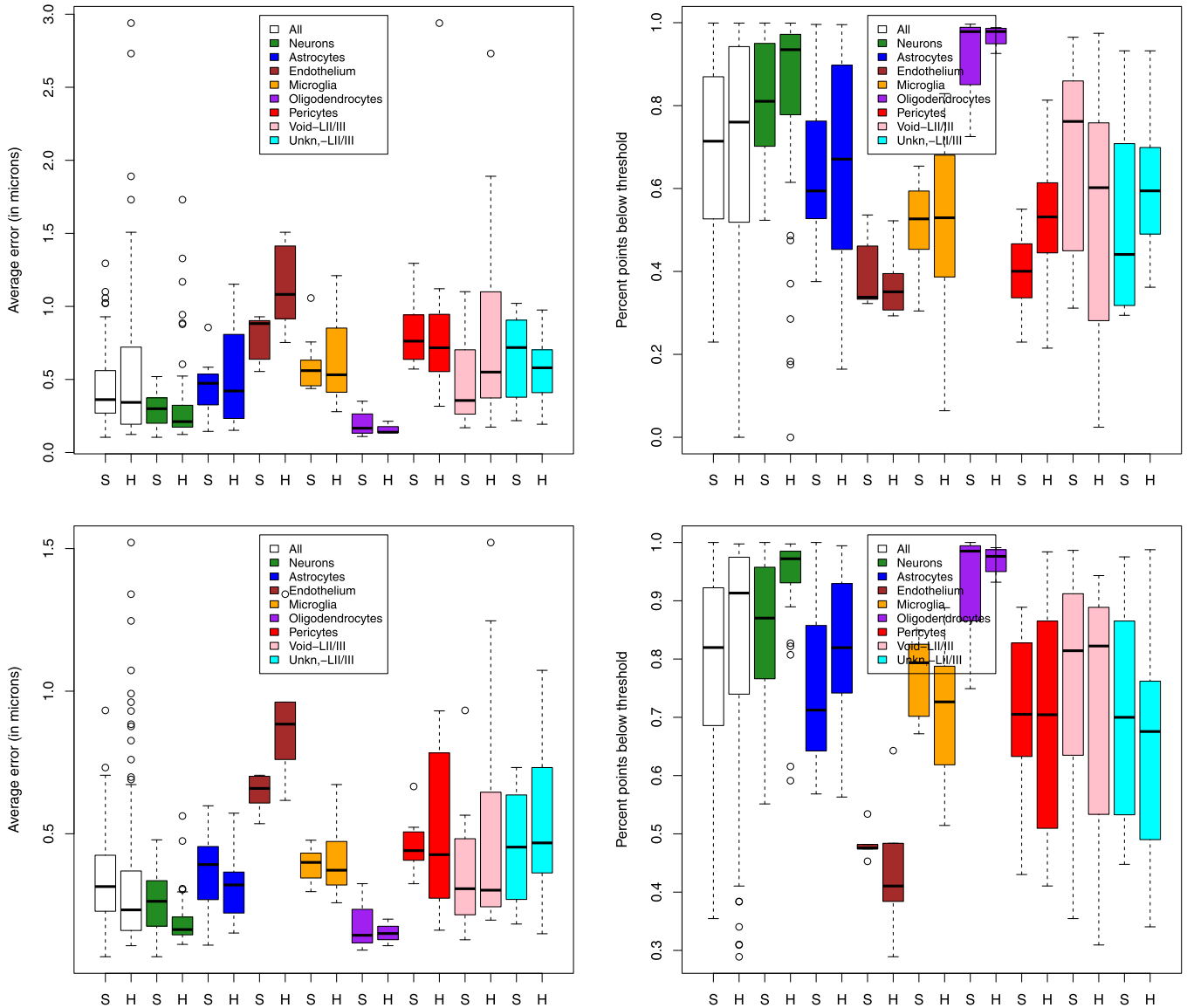


**Fig. 11. Fitting evaluation:** for two different configurations of coefficients for spherical harmonics(S) and hyperquadrics (H), we provide boxplots representing two metrics subdivided per categories: the average distance error in  $\mu$ m(left), and the percent of samples with distance error below the threshold of  $0.5\mu$ m(right). The bottom and top of each box are the first and third quartiles, the band inside the box is the second quartile (the median), and the ends of the whiskers extending vertically from the boxes represent the lowest datum still within 1.5 IQR (inter-quartile range) of the lower quartile, and the highest datum still within 1.5 IQR of the upper quartile. Outliers are indicated as small circles. Spherical harmonics are indicated with S, and Hyperquadrics are indicated with H. On top, we compare the two representations with same number of coefficients (16, for  $SH_{3,16}$  and  $HQ_{4,16}$ ), while on the bottom we compare representations with similar average accuracy ( $SH_{20,441}$  and  $HQ_{5,20}$ ).



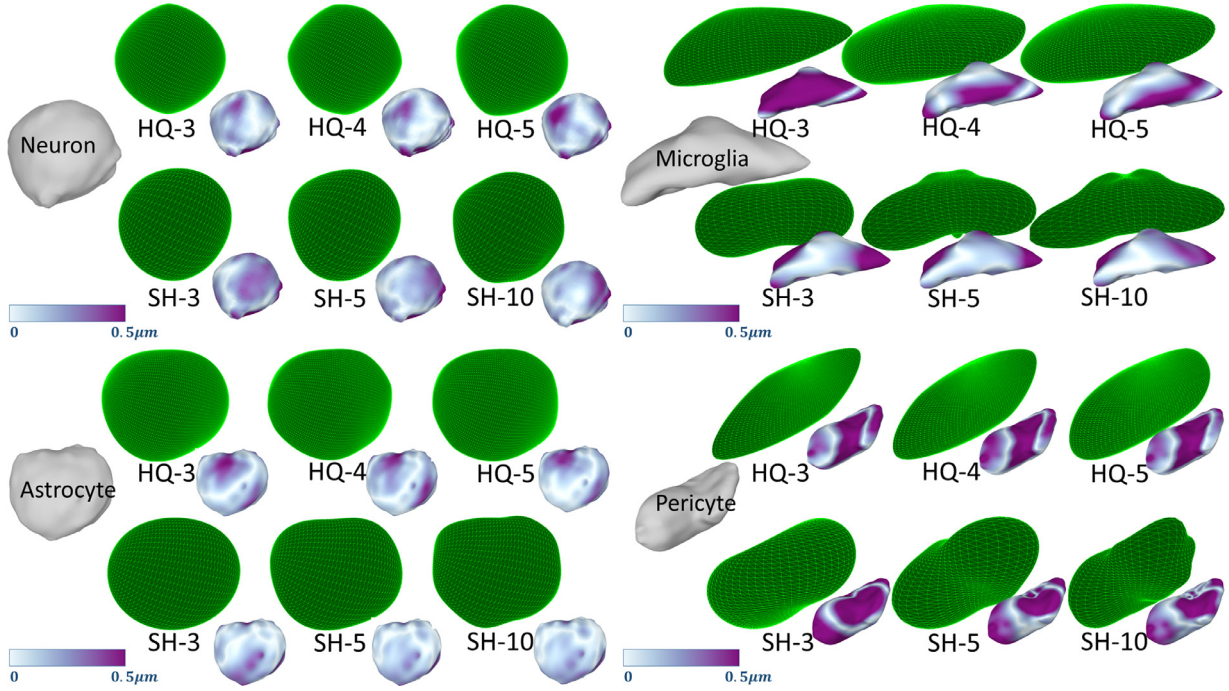


**Fig. 12.** Visual assessment of parameterizations: for nuclear shape of different categories, we show the fitting hyperquadric and spherical harmonics representations with different number of coefficients ( $HQ_{3,12}$ ,  $HQ_{4,16}$ ,  $HQ_{5,20}$ , and  $SH_{3,16}$ ,  $SH_{5,36}$ ,  $SH_{10,121}$ ). Errors are represented through BuPu Colorbrewer scheme [56]. Models are rendered using MeshLab software [57].

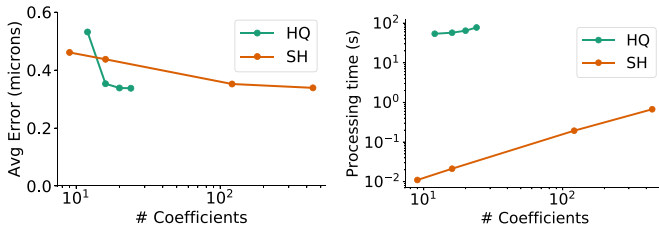


**Fig. 13.** Comparison between spherical harmonics and hyperquadrics: we compare mean accuracy (in microns) and average time processing (in seconds) with respect to the number of coefficients, for hyperquadrics and spherical harmonics representation.

we will denote the various representations as  $HQ_{N,R}$  and  $SH_{L,R}$ , where R is the number of rotation invariant coefficients.

To evaluate classification performance, we considered three cases for hyperquadrics parameterization with number of components varying from 3 to 5 (denoted as  $HQ_{3,12}$ ,  $HQ_{4,17}$ , and  $HQ_{5,22}$ ) and three cases for spherical harmonics parameterization with  $L_{\max} = 3, 10, 20$  (denoted as  $SH_{3,4}$ ,  $SH_{10,11}$ ,  $SH_{20,21}$ ). For each case, we performed grid-searching for configuring two hyperparameters for the support vector machine model, specifically the free parameter  $\gamma$  of the Gaussian radial basis function ( $K(x_i, x_j) = \exp(-\gamma \|x_i - x_j\|^2)$ ), and the constant C for weighting the soft margin regularization function.

We carried out the model training on 97 nuclear shapes of layer VI, while we left out the 24 shapes of layer II/III (Void and Unknown) for testing accuracy. Table 3 shows statistics of the usage of SVM model: for each case, we report the set of SVM hyperparameters  $\gamma$  and C, and three scores: the cross evaluation accuracy which is used for finding the best hyperparameters, the silhouette score [60] which is calculated by using the mean intra-cluster distance a and the mean nearest-cluster distance b for each sample ( $\sigma = \frac{b-a}{\max(a,b)}$ ), and the model accuracy on test shapes.

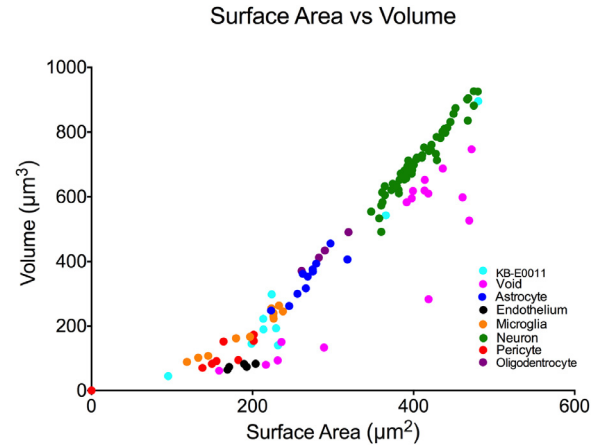


**Fig. 14.** Surface vs Volume: neuroscientists currently employ surface and volume measures to classify nuclear envelopes.

As reference, in Fig. 15, we show also how hyperparameter grid-searching performed for two cases ( $HQ_{5,22}$  on the left, and  $SH_{20,21}$  on the right). Specifically, we show cross evaluation accuracy for the set of parameters  $\gamma$  and C in the grid. From these accuracies we can infer that in our data the hyperquadric representations  $HQ_{4,17}$  and  $HQ_{5,22}$  have slightly better classification accuracy than the low order spherical harmonics representation  $SH_{3,4}$  (especially the test evaluation score). On the other hand, when the decomposition order increases, energy descriptors derived from spherical harmonics parameterization obtain higher scores for all metrics considered ( $SH_{10,11}$  and  $SH_{20,21}$ ), leading to a higher accuracy and a greater cluster separation. Unfortunately, the hyperquadric formulation is limited by not being symmetry invariant. This probably affects its classification accuracy.

**Table 3**

Support vector machine classification: Each representation determined specific classifier parameters during grid optimization. The accuracy is reported using three separate accuracy scores.

Type	SVM params	Accuracy Scores
$HQ_{3,12}$	$\gamma = 0.1$ $C = 10$	cross evaluation accuracy = 0.73 silhouette score = 0.03 test evaluation accuracy = 0.5
$HQ_{4,17}$	$\gamma = 0.1$ $C = 1$	cross evaluation accuracy = 0.75 silhouette score = 0.24 test evaluation accuracy = 0.71
$HQ_{5,22}$	$\gamma = 0.1$ $C = 10$	cross evaluation accuracy = 0.75 silhouette score = 0.16 test evaluation accuracy = 0.75
$SH_{3,4}$	$\gamma = 0.1$ $C = 1$	cross evaluation accuracy = 0.73 silhouette score = 0.29 test evaluation accuracy = 0.67
$SH_{10,11}$	$\gamma = 10^{-7}$ $C = 10^7$	cross evaluation accuracy = 0.85 silhouette score = 0.30 test evaluation accuracy = 0.67
$SH_{20,21}$	$\gamma = 10^{-7}$ $C = 10^7$	cross evaluation accuracy = 0.84 silhouette score = 0.30 test evaluation accuracy = 0.79

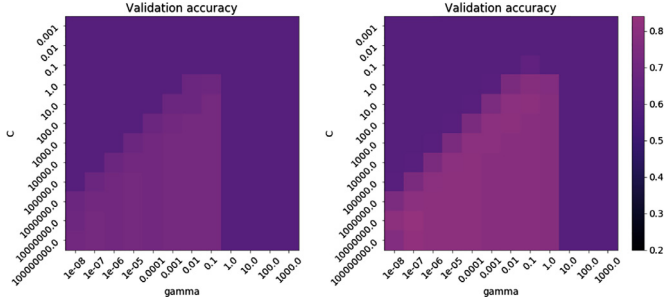


**Fig. 15.** SVM parameter optimization: we show cross evaluation accuracies for different configuration of SVM parameters  $\gamma$  and  $C$ . On left for hyperquadrics parameterization  $HQ_{5,22}$ , on the right for spherical harmonics parameterization  $SH_{20,21}$ .

### 5.2.3. Dimension reduction

In order to provide direct visual representation of the parameter data, we also considered classical dimension reduction schemes to reduce the parameter space to 2D. We used three common dimension reduction approaches:

- *Principal component analysis* which uses orthogonal transformations to convert a group of possibly correlated variables into a group of linearly uncorrelated variables called principal components. The principal components are ordered according to the variance [61,62];

- *Multidimensional scaling* which positions N-dimensional objects in a space of usually 2 or 3 dimensions by computing a square proximity matrix and by combining the largest eigenvalues and the correspondent eigenvectors [63].
- *T-distributed stochastic neighbor embedding* which models each high-dimensional object by a two- or three-dimensional point in such a way that similar objects are modeled by nearby points and dissimilar objects are modeled by distant points. This is obtained by constructing a probability distribution over pairs of high-dimensional objects, so objects have a high probability of being picked, whereas dissimilar objects have a small probability of being picked, and by defining a similar probability distribution over the points in the low-dimensional map [64].

**Fig. 16** shows the results of dimension reduction methods applied on hyperquadrics parameterization  $HQ_{5,22}$  (on the top), and spherical harmonics with  $SH_{20,21}$  (on the bottom). Visual representation of hyperquadrics and spherical harmonics appear to clearly discriminate some classes of cells, while they are not reliable for separating some other cells. In all approaches, neurons (green) form a well-defined cluster which is clearly separated from all other classes. On the bottom part of **Fig. 16**, it appears that the visual representation of spherical harmonics provides a slightly more accurate separation between the various nuclear envelope groups, and this is mostly evident when using the t-distributed stochastic neighbor embedding (on the right). Apart from a few outliers, the clusters representing the various brain cells are clearly separated

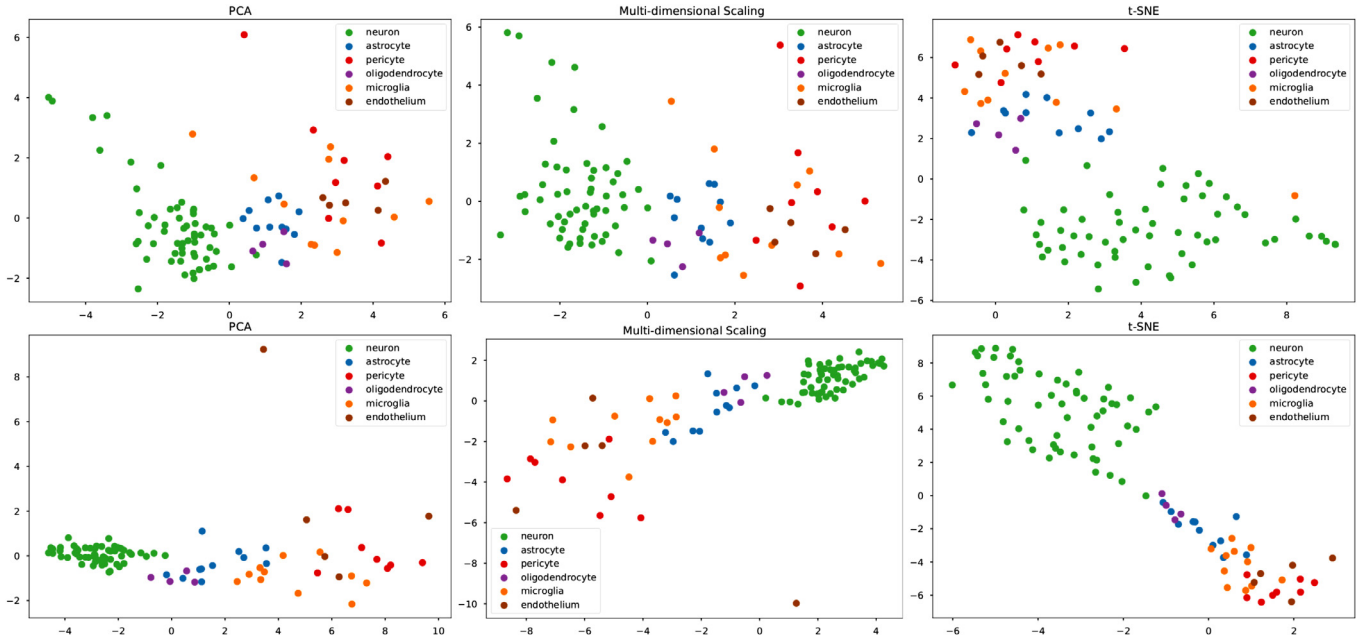


**Fig. 16.** Dimension reduction: we show three different different reduction methods used on hyperquadrics parameterization  $HQ_{5,22}$  (on the top) and on spherical harmonics parameterization  $SH_{20,21}$  (on the bottom). From left to right, Principal component analysis (PCA), multidimensional scaling (MDS), and t-distributed stochastic neighbor embedding (t-SNE). (For interpretation of the references to color in this figure, the reader is referred to the web version of this article.)

with small or negligible overlaps. These results confirm and extend the original classification performed by domain scientists that was based on the volume and area of nuclear envelopes.

## 6. Conclusions

We presented a framework for shape analysis of 3D nuclear envelopes of brain cells obtained from nanoscale digital reconstruction of mouse brain samples imaged with face-block scanning electron microscope. Our method is based on implicit and explicit parameterizations of 3D surfaces derived by adapting the classical hyperquadrics formulation [49], and the classical spherical harmonics decomposition [7].

We tested our framework on a collection of 121 brain nuclear envelopes extracted from samples of rat brain. Our results show that both parametric models can accurately represent convex neural nuclei, while the fitting performances degrade for other envelopes exhibiting concavities (specifically microglia, pericytes and endothelium). A comparison of the two parameterizations showed that a limited number of hyperquadrics components can provide an adequate shape representation, and that with the same number of coefficients, the hyperquadrics parameterization provides a slightly higher average. On the other hand, spherical harmonics fitting can be implemented as a linear least square optimization method that is orders of magnitude faster, thus making it usable with larger number of components. So, for situation where memory is not critical, spherical harmonics might be a reasonable choice, providing reasonably fast fitting together with good representation performance.

We also performed a preliminary evaluation of the proposed parameterizations as predictive models by using standard machine learning (support vector machines) and dimension reduction methods (principal component analysis, multidimensional scaling and t-distributed stochastic neighbor embedding). The preliminary analysis showed that both parameterizations can be considered reliable for discriminating neural nuclei shapes, and that, with the same fitting accuracy, a more accurate classification is obtained by considering spherical harmonics energy descriptors. In the future, we plan to explore different surface parameterizations to provide a better description of more complicated shapes. Furthermore, we plan to extend the analysis to other 3D nuclear envelope collections from different conditions, and will try classifying neurons into subtypes. Furthermore, since nuclear classification is still done by domain scientists through visual assessment of the morphology features around cells, we plan to incorporate this domain knowledge [65,66] for creating more sophisticated and accurate classifiers.

## Declaration of interests

The authors declare that they have no known competing financial interests or personal relationships that could have appeared to influence the work reported in this paper.

## Acknowledgments

This work was supported by the CRG grant no. 2313 from King Abdullah University of Science and Technology *KAUST-EPFL Alliance for Integrative Modeling of Brain Energy Metabolism*. We also acknowledge the contribution of Sardinian Regional Authorities under project VIGECLAB. We finally thank Helmut Pottmann (King Abdullah University of Science and Technology) for useful comments and suggestions.

## References

- [1] Queisser SG, Wittmann M, Bading H, Wittum G. Filtering, reconstruction, and measurement of the geometry of nuclei from hippocampal neurons based on confocal microscopy data. *J Biomed Opt* 2008;13(1):014009.
- [2] Fricker M, Hollinshead M, White N, Vaux D. Interphase nuclei of many mammalian cell types contain deep, dynamic, tubular membrane-bound invaginations of the nuclear envelope. *J Cell Biol* 1997;136(3):531–44.
- [3] Xing F, Yang L. Robust nucleus/cell detection and segmentation in digital pathology and microscopy images: a comprehensive review. *IEEE Rev Biomed Eng* 2016;9:234–63.
- [4] Wittmann M, Queisser G, Eder A, Wiegert JS, Bengtson CP, Hellwig A, et al. Synaptic activity induces dramatic changes in the geom. of the cell nucleus: interplay between nuclear structure, histone H3 phosphorylation, and nuclear calcium signaling. *J Neurosci* 2009;29(47):14687–700.
- [5] Cali C, Baghabra J, Boges DJ, Holst GR, Kreshuk A, Hamprecht FA, et al. Three-dimensional immersive virtual reality for studying cellular compartments in 3d models from em preparations of neural tissues. *J Comp Neurol* 2016;524(1):23–38.
- [6] Hanson AJ. Hyperquadrics: smoothly deformable shapes with convex polyhedral bounds. *Comput Vis Gr Image Process* 1988;44(2):191–210.
- [7] Kazhdan M, Funkhouser T, Rusinkiewicz S. Rotation invariant spherical harmonic representation of 3 D shape descriptors. In: *Proceedings of the symposium on geometry processing*, 6; 2003. p. 156–64.
- [8] Agus M, Cal C, Morales AT, Lehtsaiho HO, Magistretti PJ, Gobetti E, et al. Hyperquadrics for shape analysis of 3D nanoscale reconstructions of brain cell nuclear envelopes. In: *Livesu M, Pintore G, Signoroni A, editors. Proceedings of the smart tools and apps for graphics - eurographics Italian chapter conference. The Eurographics Association*; 2018.
- [9] Mousa M-H, Chaine R, Akkouché S, Galin E. Efficient spherical harmonics representation of 3d objects. In: *Proceedings of the fifteenth Pacific conference on computer graphics and applications*, 2007. PG'07. IEEE; 2007. p. 248–55.
- [10] Qi X, Xing F, Foran DJ, Yang L. Robust segmentation of overlapping cells in histopathology specimens using parallel seed detection and repulsive level set. *IEEE Trans Biomed Eng* 2012;59(3):754–65.
- [11] Wienert S, Heim D, Saeger K, Stenzinger A, Beil M, Hufnagl P, et al. Detection and segmentation of cell nuclei in virtual microscopy images: a minimum-model approach. *Sci Rep* 2012;2:503.
- [12] Veta M, Van Diest PJ, Kornegoor R, Huisman A, Viergever MA, Pluim JP. Automatic nuclei segmentation in H&E stained breast cancer histopathology images. *PLoS One* 2013;8(7):e70221.
- [13] Jung C, Kim C, Chae SW, Oh S. Unsupervised segmentation of overlapped nuclei using Bayesian classification. *IEEE Trans Biomed Eng* 2010;57(12):2825–32.
- [14] Vink JP, Van Leeuwen M, Van Deuren C, De Haan G. Efficient nucleus detector in histopathology images. *J Microsc* 2013;249(2):124–35.
- [15] Ali S, Madabhushi A. An integrated region-, boundary-, shape-based active contour for multiple object overlap resolution in histology imagery. *IEEE Trans Med Imaging* 2012;31(7):1448–60.
- [16] Avenel C, Kulikova MS. Marked point processes with simple and complex shape objects for cell nuclei extraction from breast cancer H&E images. *Medical Imaging 2013: Digital Pathology*, 8676; 2013. 86760Z.
- [17] Kulikova M, Veillard A, Roux L, Racocanu D. Nuclei extraction from histopathological images using a marked point process approach. In: *Proceedings of the medical imaging 2012: image processing*, 8314; 2012. p. 831428.
- [18] Ram S, Rodriguez JJ. Size-invariant detection of cell nuclei in microscopy images. *IEEE Trans Med Imaging* 2016;35(7):1753–64.
- [19] Desbrun M, Gascuel M-P. Animating soft substances with implicit surfaces. In: *Proceedings of the SIGGRAPH*; 1995. p. 287–90.
- [20] Wyvill B, Guy A, Galin E. Extending the CSG Tree. Warping, blending and boolean operations in an implicit surface modeling system. In: *Computer graphics forum*, 18; 1999. p. 149–58.
- [21] Loop C, Blinn J. Real-time GPU rendering of piecewise algebraic surfaces. *ACM Trans. Gr* 2006;25:664–70.
- [22] Singh JM, Narayanan P. Real-time ray tracing of implicit surfaces on the GPU. *IEEE Trans Vis Comput Gr* 2010;16(2):261–72.
- [23] Hadwiger M, Sigg C, Scharsach H, Bühler K, Gross M. Real-time ray-casting and advanced shading of discrete isosurfaces. In: *Computer graphics forum*, 24; 2005. p. 303–12.
- [24] Parulek J, Viola I. Implicit representation of molecular surfaces. In: *Proceedings of the visualization symposium (PacificVis)*; 2012. p. 217–24.
- [25] Hermosilla P, Krone M, Gualar V, Vázquez P-P, Vinacua À, Ropinski T. Interactive GPU-based generation of solvent-excluded surfaces. *Vis Comput* 2017;33(6–8):869–81.
- [26] Barr AH. Superquadrics and angle-preserving transformations. *IEEE Comput Gr Appl* 1981;1(1):11–23.
- [27] Pentland AP. Perceptual organization and the representation of natural form. *Artif Intell* 1986;28(3):293–331.
- [28] Solina F, Bajcsy R. Recovery of param. Models from range images: The case for superquadrics with global deform. *IEEE Trans Pattern Anal Mach Intell* 1990;12(2):131–47.
- [29] Gupta A, Bajcsy R. Volumetric segmentation of range images of 3D objects using superquadric models. *CVGIP: Image Underst.* 1993;58(3):302–26.
- [30] Terzopoulos D, Metaxas D. Dynamic 3d models with local and global deformations: Deformable superquadrics. In: *Proceedings of the third international conference on computer vision*. IEEE; 1990. p. 606–15.



- [31] Han S, Goldgof DB, Bowyer KW. Using hyperquadrics for shape recovery from range data. In: *Proceedings of the ICCV*; 1993. p. 492–6.
- [32] Cohen I, Cohen LD. A hybrid hyperquadric model for 2-D and 3-D data fitting. *Comput Vis Image Underst* 1996;63(3):527–41.
- [33] Cong G, Parvin B. Model-based segmentation of nuclei. *Pattern Recognit* 2000;33(8):1383–93.
- [34] Brechbühler C, Gerig G, Kübler O. Parametrization of closed surfaces for 3-D shape description. *Comput Vis Image Underst* 1995;61(2):154–70.
- [35] Ng B, Toews M, Durrleman S, Shi Y. Shape analysis for brain structures. In: *Shape analysis in medical image analysis*. Springer; 2014. p. 3–49.
- [36] Wachinger C, Golland P, Kremen W, Fischl B, Reuter M, et al. Brainprint: a discriminative characterization of brain morphology. *NeuroImage* 2015;109:232–48.
- [37] Härtel S, Jara J, Lemus C, Concha M. 3D morphotopological analysis of asymmetric neuronal morphogenesis in developing zebrafish. *Comput Model Objects Represent Images Fundam Methods Appl* 2018;6:215–20.
- [38] Shen L, Farid H, McPeck MA. Modeling three-dimensional morphological structures using spherical harmonics. *Evol Int J Organ Evol* 2009;63(4):1003–16.
- [39] Shi J, Zhang W, Wang Y. Shape analysis with hyperbolic Wasserstein distance. In: *Proceedings of the IEEE conference on computer vision and pattern recognition*; 2016. p. 5051–61.
- [40] Xiao P, Barnes N, Caetano T. 3-D shape matching and non-rigid correspondence for hippocampi based on Markov random fields. *IEEE Trans Image Process* 2018;27(3):1271–81.
- [41] Knott G, Marchman H, Wall D, Lich B. Serial section scanning electron microscopy of adult brain tissue using focused ion beam milling. *J Neurosci* 2008;28(12):2959–64.
- [42] Thévenaz P, Ruttimann U, Unser M. A pyramid approach to subpixel registration based on intensity. *IEEE Trans Image Process* 1998;7(1):27–41.
- [43] Kaynig V, Vazquez-Reina A, Knowles-Barley S, Roberts M, Jones TR, Kasthuri N, et al. Large-scale automatic reconstruction of neuronal processes from electron microscopy images. *Med Image Anal* 2015;22(1):77–88.
- [44] Cardona A, Saalfeld S, Schindelin J, Arganda-Carreras I, Preibisch S, Longair M, et al. Trakem2 software for neural circuit reconstruction. *PloS One* 2012;7(6):e38011.
- [45] Sommer C, Straehle C, Köthe U, Hamprecht FA. Ilastik: interactive learning and segmentation toolkit. In: *Proceedings of the IEEE international symposium on biomedical imaging: From nano to macro*. IEEE; 2011. p. 230–3.
- [46] Coggan JS, Cali C, Keller D, Agus M, Boges D, Abdellah M, et al. A process for digitizing and simulating biologically realistic oligocellular networks demonstrated for the neuro-glio-vascular ensemble. *Front Neurosci* 2018;12:664.
- [47] Holst G, Berg S, Kare K, Magistretti P, Cali C. Adding large em stack support. In: *Proceedings of the Saudi International Conference on Information Technology (Big Data Analysis)(KACSTIT)*. IEEE; 2016. p. 1–7.
- [48] Treece GM, Prager RW, Gee AH. Regularised marching tetrahedra: improved ISO-surface extraction. *Comput Gr* 1999;23(4):583–98.
- [49] Ohuchi M, Saito T. Three-dimensional shape modeling with extended hyperquadrics. In: *Proceedings of the third International Conference on 3-D digital imaging and modeling*. IEEE; 2001. p. 262–9.
- [50] Lourakis MI. A brief description of the Levenberg-Marquardt algorithm implemented by Levmar. *Found Res Technol* 2005;4(1):1–6.
- [51] Kumar S, Han S, Goldgof D, Bowyer K. On recovering hyperquadrics from range data. *IEEE Trans Pattern Anal Mach Intell* 1995;17(11):1079–83.
- [52] Guarda AFR, Bioucas-Dias JM, Rodrigues NMM, Pereira F. Improving point cloud to surface reconstruction with generalized Tikhonov regularization. In: *Proceedings of the IEEE nineteenth international workshop on multimedia signal processing (MMSP)*; 2017. p. 1–6. doi:10.1109/MMSP.2017.8122287.
- [53] Guennebaud G, Jacob B., et al. Eigen. <http://eigen.tuxfamily.org> 2010.
- [54] Grüning BA, Rasche E, Rebolledo-Jaramillo B, Eberhard C, Houwaart T, Chilton J, et al. Jupyter and galaxy: easing entry barriers into complex data analyses for biomedical researchers. *PloS Comput Biol* 2017;13(5):e1005425.
- [55] Pedregosa F, Varoquaux G, Gramfort A, Michel V, Thirion B, Grisel O, et al. Scikit-learn: machine learning in python. *J Mach Learn Res* 2011;12(Oct):2825–30.
- [56] Harrower M, Brewer CA. Colorbrewer.org: an online tool for selecting colour schemes for maps. *Cartogr J* 2003;40(1):27–37.
- [57] Cignoni P, Callieri M, Corsini M, Dellepiane M, Ganovelli F, Ranzuglia G. MeshLab: an Open-Source Mesh Processing Tool. In: *Proceedings of the Eurographics Italian chapter conference*; 2008. p. 1–8.
- [58] Platt J, et al. Probabilistic outputs for support vector machines and comparisons to regularized likelihood methods. *Adv Large Margin Classif* 1999;10(3):61–74.
- [59] Wu T-F, Lin C-J, Weng RC. Probability estimates for multi-class classification by pairwise coupling. *J Mach Learn Res* 2004;5:975–1005. <http://dl.acm.org/citation.cfm?id=1005332.1016791>.
- [60] Rousseeuw PJ. Silhouettes: a graphical aid to the interpretation and validation of cluster analysis. *J Comput Appl Math* 1987;20:53–65.
- [61] Einasto M, Liivamägi L, Saar E, Einasto J, Tempel E, Tago E, et al. Sdss dr7 superclusters-principal component analysis. *Astron Astrophys* 2011;535:A36.
- [62] Shlens J. A tutorial on principal component analysis. *arXiv:1404.1100* 2014.
- [63] Kruskal JB. Multidimensional scaling by optimizing goodness of fit to a non-metric hypothesis. *Psychometrika* 1964;29(1):1–27.
- [64] Maaten Lvd, Hinton G. Visualizing data using T-SNE. *J Mach Learn Res* 2008;9(Nov):2579–605.
- [65] Armañanzas R, Ascoli GA. Towards the automatic classification of neurons. *Trends Neurosci* 2015;38(5):307–18.
- [66] Zeng H, Sanes JR. Neuronal cell-type classification: challenges, opportunities and the path forward. *Nat Rev Neurosci* 2017;18(9):530.